



Storm Track Response to Oceanic Eddies in Idealized Atmospheric Simulations

A. FOUSSARD

LMD/IPSL, CNRS, Ecole Polytechnique, Ecole Normale Supérieure, Sorbonne Université, Paris, and Ecole des Ponts ParisTech, Champs-sur-Marne, France

G. LAPEYRE AND R. PLOUGONVEN

LMD/IPSL, CNRS, Ecole Polytechnique, Ecole Normale Supérieure, Sorbonne Université, Paris, France

(Manuscript received 27 June 2018, in final form 17 September 2018)

ABSTRACT

Large-scale oceanic fronts, such as in western boundary currents, have been shown to play an important role in the dynamics of atmospheric storm tracks. Little is known about the influence of mesoscale oceanic eddies on the free troposphere, although their imprint on the atmospheric boundary layer is well documented. The present study investigates the response of the tropospheric storm track to the presence of sea surface temperature (SST) anomalies associated with an eddying ocean. Idealized experiments are carried out in a configuration of a zonally reentrant channel representing the midlatitudes. The SST field is composed of a large-scale zonally symmetric front to which are added mesoscale eddies localized close to the front. Numerical simulations show a robust signal of a poleward shift of the storm track and of the tropospheric eddy-driven jet when oceanic eddies are taken into account. This is accompanied by more intense air–sea fluxes and convective heating above oceanic eddies. Also, a mean heating of the troposphere occurs poleward of the oceanic eddying region, within the storm track. A heat budget analysis shows that it is caused by a stronger diabatic heating within storms associated with more water advected poleward. This additional heating affects the baroclinicity of the flow, which pushes the jet and the storm track poleward.

1. Introduction

External factors acting on the dynamics of the midlatitude storm tracks in terms of variability and evolution with climate change are still poorly understood (Chang et al. 2002; Shaw et al. 2016). Tropical forcing induced by sea surface temperature (SST) anomalies as can occur during ENSO events has been shown to have a clear influence on the midlatitudes. Warm SSTs enhance convection in the tropics and generate large-scale Rossby wave trains propagating toward the poles (Held et al. 1989; Lau 1997; Cassou and Terray 2001; Shapiro et al. 2001). The Hadley cell contributes as well to the midlatitude variability through the interaction between the subtropical jet stream and the midlatitude eddy-driven jet (e.g., Lee and Kim 2003; Michel and Rivière 2014). The stratosphere is another element affecting the storm-track variability through mechanisms

such as the so-called downward control (e.g., Kidston et al. 2015).

In the midlatitudes, large-scale SST anomalies were believed for a long time to play a minor role in the storm-track dynamics (Lau 1997; Robinson 2000; Kushnir et al. 2002). However it has been recently recognized that these SST anomalies were in fact affecting the atmosphere, not through their large-scale spatial structure, but rather through their frontal signature (Nakamura et al. 2004; Minobe et al. 2008). This new conception has led to original findings explaining the link between the observed variability of western boundary currents and the variability of the storm tracks (Smirnov et al. 2015; Révelard et al. 2016). In particular, deep convection intensifies above the warm flank of the front (Minobe et al. 2008; Tokinaga et al. 2009) with a locally stronger storm track at low levels (Small et al. 2014) along with more explosive cyclogenesis (Kuwano-Yoshida and Minobe 2017). In addition to these local effects, a large-scale downstream response in terms of eddy-driven jet position or weather regimes develops in the Pacific

Corresponding author address: G. Lapeyre, glapeyre@lmd.ens.fr

DOI: 10.1175/JCLI-D-18-0415.1

© 2018 American Meteorological Society. For information regarding reuse of this content and general copyright information, consult the [AMS Copyright Policy](https://www.ametsoc.org/PUBSReuseLicenses) (www.ametsoc.org/PUBSReuseLicenses).

(Frankignoul et al. 2011; O'Reilly and Czaja 2015), the Atlantic region (Piazza et al. 2016; O'Reilly et al. 2017), or the Southern Ocean (Nakamura et al. 2004).

Even if processes connecting SST fronts and storm-track dynamics are beginning to be well understood (e.g., Nakamura et al. 2008; Brayshaw et al. 2008; Sampe et al. 2010; Graff and LaCasce 2012), other questions have still to be addressed. One is related to the presence of oceanic mesoscale eddies (of a typical diameter of 100 km) that populate the World Ocean (Chelton et al. 2011). Observational and numerical studies have shown that these structures affect the atmospheric boundary layer (e.g., Bourras et al. 2004; Lambaerts et al. 2013; Chelton et al. 2004; Frenger et al. 2013). This occurs through air–sea heat fluxes modulated by oceanic eddies (Bourras et al. 2004; Villas Bôas et al. 2015), with a response of atmospheric stability to SST anomalies (O'Neill 2012), and through wind stress modification by ocean currents (Renault et al. 2016). A natural question that arises concerns the vertical extent of the atmospheric response and its impact at large scales.

Ma et al. (X. Ma et al. 2015; Ma et al. 2017) have investigated the remote effect of oceanic eddies on the North Pacific storm track. They showed the existence of a large-scale atmospheric response through the Pacific, down to the west coast of North America. However, responses to oceanic forcings in general strongly depend on the basic state (Peng and Robinson 2001; Kushnir et al. 2002). The sensitivity of the response to oceanic eddies may thus depend, as well, on the mid-latitude ocean basin considered with its associated storm track, or the climatology of the mean state for a particular season.

In the present paper, we reconsider the influence of oceanic eddies through their SST anomalies on the atmospheric storm tracks using an approach based on idealized experiments. To this end, we examine the response to an ocean filled with oceanic eddies (stationary in time) in a channel geometry representing mid-latitudes with zonal symmetry. One advantage of this geometry is that atmospheric synoptic disturbances will be affected by oceanic eddies regardless of their stage of development, a situation typical for the Southern Ocean. The structure of the paper is as follows. Section 2 describes the configuration of simulations used to unveil the sensitivity of the storm track to oceanic eddies. In section 3, we discuss the basic properties of the control experiment and present some characteristics of the experiment with oceanic eddies. Section 4 is devoted to the main results of this study (i.e., the determination of the response of the atmospheric storm track to oceanic eddies). Then we explore the underlying mechanisms in section 5. Final conclusions are drawn in section 6.

2. Experimental design

a. Model configuration

We use version 3.6.1 of the WRF Model (Skamarock et al. 2008) with parameterizations for microphysics (Kessler scheme), convection (Kain and Fritsch scheme), and radiative exchanges (presented below). The nonlocal Yonsei University (YSU) parameterization is used for the atmospheric boundary layer, with a scheme based on Monin–Obukhov similarity theory for the surface layer (MM5 similarity revised scheme).

The domain is a Cartesian channel of size $L_x \times L_y = 9216 \text{ km} \times 9216 \text{ km}$ with a horizontal resolution of 18 km. It is periodic in the x direction, with free slip boundary conditions in the y direction. Coordinates x and y will serve as zonal and meridional directions respectively, with a Northern Hemisphere orientation. Fifty η levels are used for the hydrostatic-pressure vertical coordinate, with a domain top at 36 hPa. A modified β plane is used (detailed in appendix A), and the Coriolis parameter at the center of the domain equals its value at 40°N .

The model is forced through surface exchanges with fixed SST and through radiative processes that are also related to the SST field. Radiative exchanges are represented with a single-column gray-radiation model following Frierson et al. (2006), with a single wavelength for longwave radiative fluxes, transparent to water vapor and clouds. Such a simple radiative forcing eliminates the extra dependence of the forcing on water vapor, only keeping the dependence on SST. A detailed description is presented in appendix B.

The CTRL experiment is associated with a zonally homogeneous SST, fixed in time, representing a large-scale front (Fig. 1a). Its profile is given by

$$\text{SST}_{\text{CTRL}}(y) = \text{SST}_{\text{front}} - \frac{\Delta\text{SST}}{2} \tanh\left(\frac{y - y_{\text{sst}}}{l_{\text{sst}}}\right).$$

Sea surface temperature varies between 275 and 295 K, and the SST front is centered at $y_{\text{sst}} = 4500 \text{ km}$. Other parameters are listed in Table 1.

b. EDDY experiment

The same atmospheric configuration is used for the EDDY experiment, changing only the SST field. Compared to CTRL, an eddy component $\text{SST}_{\text{eddies}}(x, y)$ is added. It aims to represent oceanic mesoscale structures (of a typical size of 100–500 km), resulting for instance from the dynamical instability of the oceanic front. They are artificially obtained from a snapshot of a 2D turbulent field $F(x, y)$ of a surface quasigeostrophic model (Lapeyre and Klein 2006) for a domain size of

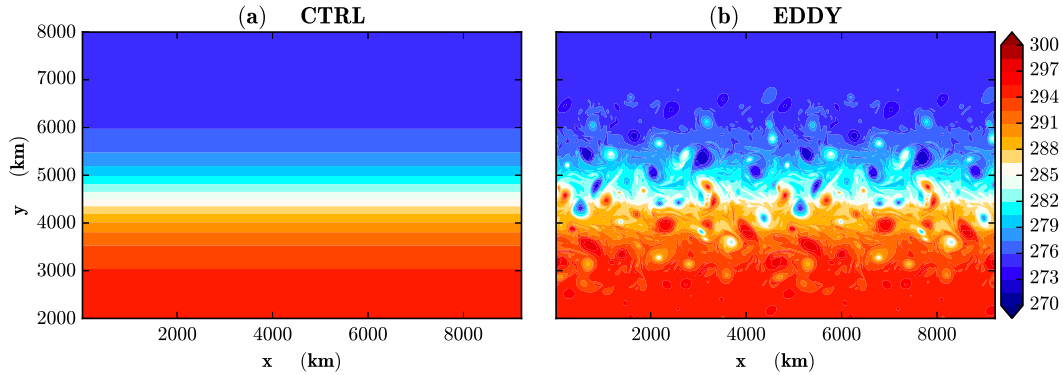


FIG. 1. SST fields (K). (a) CTRL and (b) EDDY experiments.

$L_x/2 \times L_y/2$ and extended by periodicity to the full domain. To define $SST_{\text{eddies}}(x, y)$, its zonal mean is subtracted, and it is normalized to get a maximum standard deviation of 3 K. Then it is multiplied by a Gaussian envelope $G(y) = \exp[-(y - y_{\text{sst}})^2/l_{\text{an}}^2]$ to locate eddy structures near the core of the large-scale front. The SST field ultimately used for EDDY experiment is then defined as

$$SST_{\text{EDDY}}(x, y) = SST_{\text{CTRL}}(y) + SST_{\text{eddies}}(x, y)$$

and is shown in Fig. 1b. With this method, the same SST zonal average is obtained for the EDDY and CTRL experiments. This technique contrasts with other approaches that rely on isotropic or partially anisotropic spatial filtering of SST (Woollings et al. 2010; Small et al. 2014; Ma et al. 2017). In particular, it allows us to discard potential additional effects due to modifications of the cross-front SST gradient.

c. Statistical methodology

A first simulation with SST_{CTRL} is run for 4 years starting from radiative equilibrium. We then run six pairs of simulations (CTRL and EDDY) of 4-yr durations starting from different initial conditions. For each, we discarded the first 3 months and computed the time and ensemble average.

We applied a Wilcoxon rank test performed on annual and zonal means of any given quantity to assess the statistical significance of differences between EDDY and CTRL. The underlying hypothesis is that each 1-yr-mean EDDY – CTRL difference corresponds to an independent realization without any requirement on the Gaussian character of the differences distribution. This test is used to identify regions where the hypothesis of having a distribution of the EDDY – CTRL differences symmetric around zero can be rejected with a high confidence, here with a threshold of 95%. Classical

Student's t tests, assuming a normal distribution of each variable, give similar results (not shown).

3. Basic properties of CTRL and EDDY experiments

a. Mean state of the CTRL experiment

Figure 2 summarizes the mean state (in the sense of zonal and time average) of the storm track for the CTRL experiment. In the following, the notation $\langle \rangle$ stands for a zonal average, and $\overline{(\)}$ for a time average. We also introduce the notation $(\)'$ for bandpass filtered variables in the synoptic range using a 2–10-day Lanczos filter with a 31-day large window (Duchon 1979).

The zonal wind maximum (around 25 m s^{-1}) is located around $y = 6000 \text{ km}$, below the tropopause, and extends down to the surface (Fig. 2a). Weak mean easterlies lie in the lowest layers on the warm side of the SST front around $y = 3500 \text{ km}$. The tropopause height changes from 200 hPa on the equatorial side of the domain down to 400 hPa on the poleward side (not shown). The meridional eddy heat flux $\langle v'T' \rangle$ (shading in Fig. 2a) is oriented toward the pole over the whole domain and is at a maximum poleward of the oceanic front at an altitude around 750 hPa.

Specific humidity is at a maximum at the surface on the warm side of the domain, reaching values larger than 10 g kg^{-1} (contours in Fig. 2b) and decreases both with

TABLE 1. Numerical values used in the WRF simulations.

Parameter	Value
$L_x = L_y$	9216 km
$(y_{\text{sst}}, l_{\text{sst}})$	(4500 km, 1000 km)
$(SST_{\text{front}}, \Delta SST)$	(285 K, 20 K)
$\Delta\theta$	10 K
P_0	1013 hPa
f_0	$9.35 \times 10^{-5} \text{ s}^{-1}$
β_{max}	$1.75 \times 10^{-11} \text{ s}^{-1} \text{ m}^{-1}$
$l_{\text{an}} = l_{\beta}$	1500 km

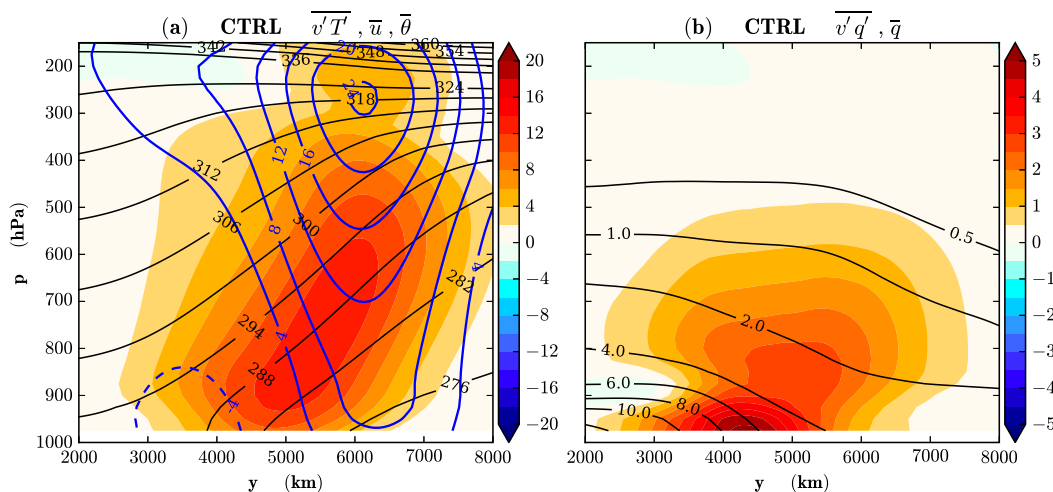


FIG. 2. Storm-track properties of the CTRL experiment. (a) Zonal wind (blue contours; m s^{-1}), (2–10 days filtered) meridional flux of temperature (shading; K m s^{-1}) and potential temperature (black contours; K). (b) Specific humidity (contours; g kg^{-1}) and (2–10 days filtered) meridional flux of specific humidity (shading; $\text{g kg}^{-1} \text{m s}^{-1}$).

latitude and altitude. Synoptic transients (2–10 days) account for about half of the poleward specific humidity flux with two local maxima, one in the boundary layer below 900 hPa where the SST front is the strongest and a second one in the free troposphere slightly poleward at 850 hPa (shading in Fig. 2b).

b. Instantaneous fields in presence of oceanic eddies

Figure 3 illustrates a typical situation of a surface storm above the oceanic eddies in the EDDY experiment. First, high values of SST anomalies are found in oceanic structures with a diameter around 300 km (Fig. 3a). The atmospheric temperature field and specific humidity at 700 hPa are shown in Fig. 3b. Warm and cold atmospheric fronts are visible, with their typical high temperature gradients and high values of specific humidity. However, when compared with Fig. 3a, we do not detect the imprint of the oceanic eddies on these quantities at this altitude. The surface 10-m wind speed (Fig. 3c) is intensified along the cold front, as well as near the storm center, associated with a cyclonic circulation. Again no signature of oceanic eddies is found in this instantaneous field. This contrasts with its time average where a clear wind–SST coupling is found (A. Foussard et al. 2018, unpublished manuscript).

Figure 3d shows the surface sensible heat flux from the ocean to the atmosphere. Its large-scale organization is linked to the synoptic variations of atmospheric temperature, with a positive heat flux behind the atmospheric cold front, and a negative one behind the warm front. At smaller scales, it partially correlates with the SST anomalies. This is most apparent behind the cold front where the air–sea temperature difference is the

highest (cf. Figs. 3a and 3d around $x = 2000$ and $y = 5000$ km).

Figure 3e shows the diabatic heating due to convection, microphysics, and boundary layer processes vertically integrated between 300 and 900 hPa. From now on, the term “diabatic heating” implies that radiative heating or cooling is excluded. Large amounts of heating occur along the synoptic fronts as well as near the storm center. As with specific humidity, there is no clear evidence of a direct link with the eddy SST field. The same remarks can be made for the rain rate integrated over 24 h, which only reflects the synoptic variability (Fig. 3f). We conclude that, above the boundary layer, synoptic variability is the dominant process to set the spatial distribution of humidity, temperature, and diabatic heating.

4. Atmospheric response to oceanic eddies

a. Sensitivity of surface fluxes to local SST anomalies

To assess the quality of our simulation in reproducing the response of the atmospheric boundary layer to SST anomalies, we first determine the sensitivity of air–sea fluxes to SST anomalies. It consists in computing a linear regression of time-mean sensible and latent heat fluxes, after removing their zonal mean (i.e., $F_{\text{SENS}} - \langle F_{\text{SENS}} \rangle$ and $F_{\text{LAT}} - \langle F_{\text{LAT}} \rangle$) onto $\text{SST}_{\text{eddies}}$. Regression coefficients are 12.9 and $24.8 \text{ W m}^{-2} \text{ K}^{-1}$ for sensible and latent heat fluxes, respectively (see Table 2). These values compare well with the ones obtained for realistic wintertime coupled atmospheric simulations or reanalyses (Byrne et al. 2015; Ma et al. 2016).

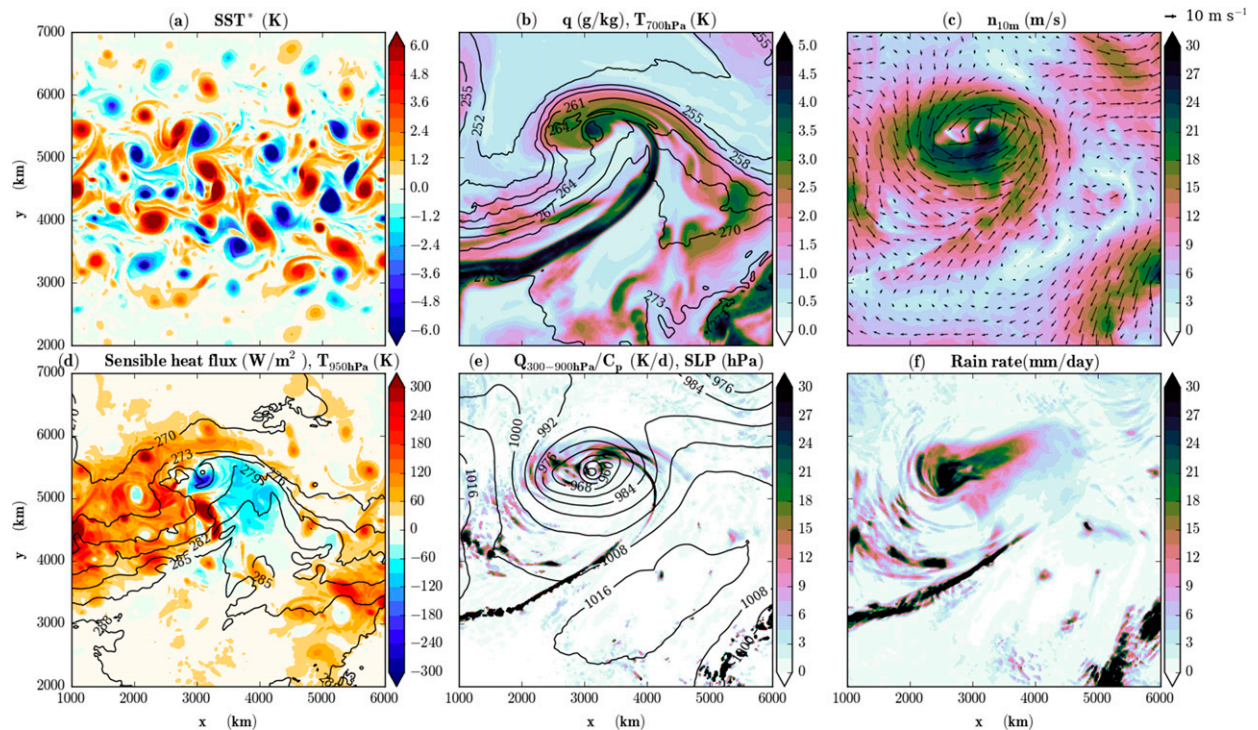


FIG. 3. Maps of various fields illustrating one storm for the EDDY simulation. (a) SST anomalies (SST_{eddies} ; K). (b) Snapshots of temperature at 700 hPa (contours; K) and specific humidity at 700 hPa (shading; g kg^{-1}). (c) 10-m wind speed (m s^{-1}) and wind vectors. (d) Temperature at 950 hPa (contours; K), and air–sea sensible heat flux (shading; W m^{-2} , positive upward). (e) Sea level pressure (contours; hPa) and diabatic heating vertically averaged between 300 and 900 hPa (shading; K day^{-1}). (f) Rain rate, averaged over a 24-h interval (mm day^{-1}).

When separating positive and negative SST anomalies, we find that the sensitivity to positive SST anomalies is larger than the sensitivity to negative SST anomalies (Table 2), as previously noted by X. Ma et al. (2015). Reduced stability over warm eddies is one of the possible explanations of this nonlinearity. Also, the nonlinearity of saturation mixing ratio with respect to SST may play a role for the latent heat flux but a precise quantification has not been done here.

Concerning the wind–SST coupling (Chelton et al. 2004; Frenger et al. 2013), it is also correctly reproduced down to the smallest resolved scales as discussed by Plougonven et al. (2018) and A. Foussard et al. (2018, unpublished manuscript). Local variations of time-mean precipitation are especially pronounced above warm eddies on the warm flank of the oceanic front and are dominated by a deep convective heating extending up to 400 hPa (not shown). This deep convection in the time average over oceanic eddies is consistent with local increase in CAPE above warm SST anomalies (X. Ma et al. 2015; Vanni re et al. 2017). Over the region with oceanic eddies ($3600 \leq y \leq 5400$ km), the rain–SST sensitivity is about $0.52 \text{ mm day}^{-1} \text{ K}^{-1}$ (considering deviations from the zonal mean), with a correlation coefficient between rain and

SST of 0.68. This sensitivity is of the same order with values found for the Kuroshio Extension region by J. Ma et al. (2015) in reanalyses (about $0.7 \text{ mm day}^{-1} \text{ K}^{-1}$) or by Liu et al. (2018) in satellite data (about $0.5 \text{ mm day}^{-1} \text{ K}^{-1}$ in winter). However, it is much larger than values found by Frenger et al. (2013) or Byrne et al. (2015) of about $0.2 \text{ mm day}^{-1} \text{ K}^{-1}$ for eddies in the Antarctic Circumpolar Current, possibly due to a colder SST.

b. Average response of surface fluxes

In addition to a response of surface fluxes at the scale of the oceanic eddies, we expect from Table 2 a net

TABLE 2. Sensitivity of surface fluxes to SST anomalies ($\text{W m}^{-2} \text{ K}^{-1}$) computed by a linear regression of the deviation from zonal mean of time-averaged heat fluxes onto SST anomalies. The regression coefficient is computed over different ranges of SST anomalies.

Anomaly range	Latent flux	Sensible flux
–4 to 4 K	24.8	12.9
–4 to 0 K	19.4	10.3
0 to 4 K	33.1	16.5

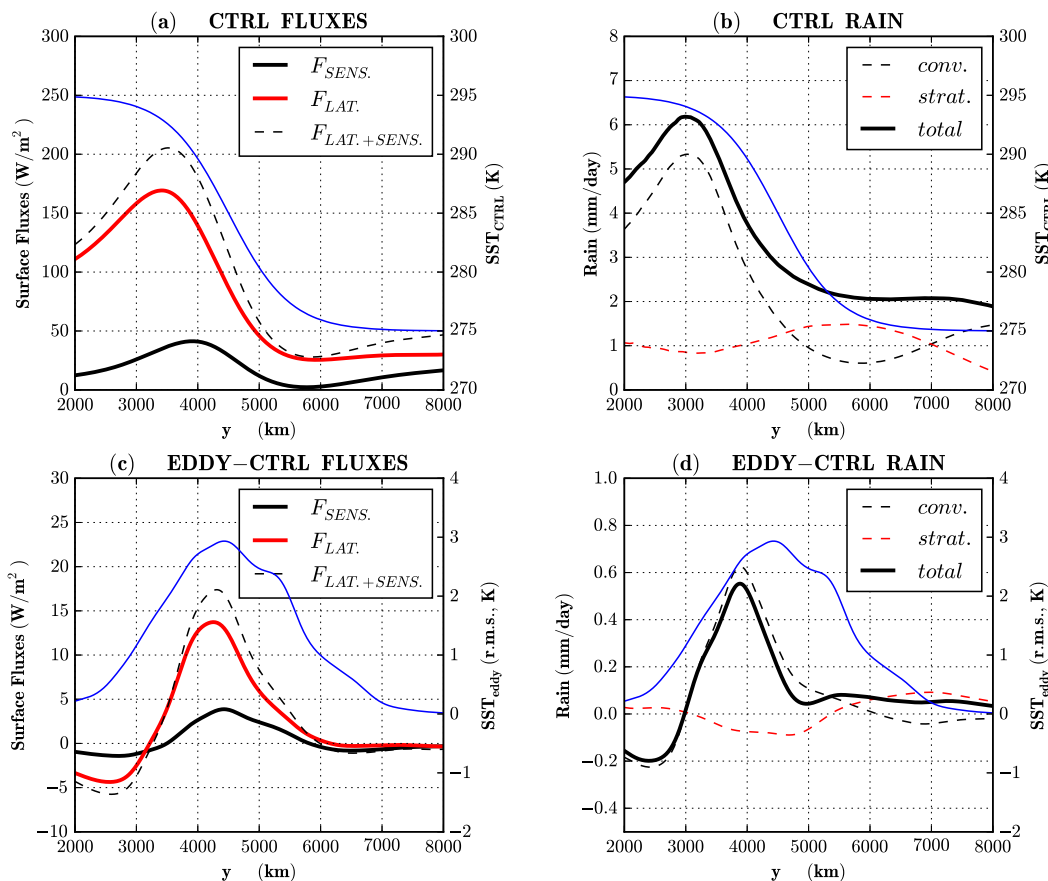


FIG. 4. (a),(b) CTRL experiment and (c),(d) differences between EDDY and CTRL, showing (left) zonal and time averages of surface turbulent heat fluxes (W m^{-2}): latent heat (red curve), sensible heat (black curve), and total flux (black dashed curve), and (right) zonal and time averages of precipitation rates (mm day^{-1} ; thick black curve) separated between convective (thin dashed black curve) and stratiform (thin dashed red curve) components. The blue curve in (a) and (b) is SST_{CTRL} (K) and in (c) and (d) is $\langle SST_{eddy}^2 \rangle^{1/2}$ (K). In (c) and (d), quantities are convolved by a Gaussian kernel $G(y) = \exp(-y^2/r^2)$ with $r = 300$ km.

effect at larger scales when numerous eddies are present. Figure 4a shows the surface sensible and latent heat fluxes, $\langle F_{SENS} \rangle$, $\langle F_{LAT} \rangle$, as a function of latitude for the CTRL experiment. Surface turbulent heat fluxes are at a maximum above the warm side of the oceanic front, reaching values about 200 W m^{-2} . Figure 4c shows the EDDY – CTRL difference after filtering out the smallest latitudinal variations, by convolution with a Gaussian kernel of meridional radius 300 km. Within the region of oceanic eddies (between $y = 3500$ and 5500 km), both sensible and latent heat fluxes increase by 10% compared to CTRL, the major part of it being related to surface evaporation. This increase in heat fluxes can be related to local effects over oceanic eddies. Warm SST anomalies generate positive anomalies of heat fluxes, stronger than the negative ones generated by cold SST anomalies (Table 2). As a result, there is a net surface heating of the atmosphere on the

order of 18 W m^{-2} for an SST rms on the order of 3 K. Equatorward of $y = 3000$ km, there is a reduction in heat fluxes compared to CTRL, probably due to a modification of the surface winds or surface temperature at these latitudes through a large-scale response of the atmospheric circulation.

Figure 4b shows the time-mean precipitation for CTRL. Precipitation rate peaks slightly equatorward of the SST front, reaching 6 mm day^{-1} mainly due to convection. North of $y = 5000$ km, in the storm-track region, typical values are on the order of 2 mm day^{-1} , with a larger contribution of stratiform precipitation. The difference between EDDY and CTRL exhibits an increase in total precipitation on the warm side of the eddy region ($3000 < y < 5000$ km) reaching 0.6 mm day^{-1} with a decrease for $y < 3000$ km (Fig. 4d). Both variations are almost entirely attributed to convective precipitation. For latitudes $y < 3000$ km, the decrease in precipitation

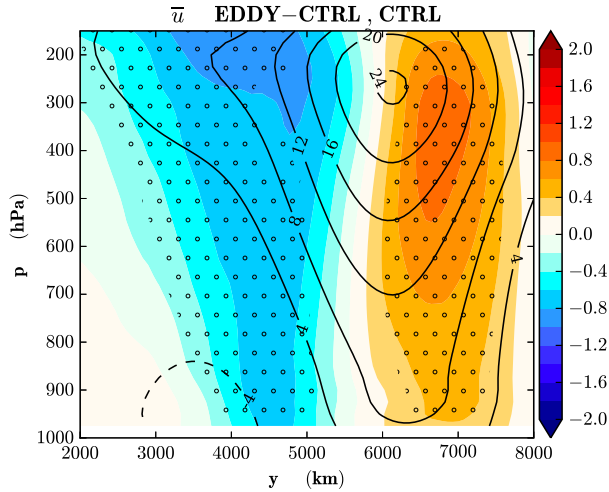


FIG. 5. Zonal and time average of zonal wind (m s^{-1}) showing the CTRL experiment (contours) and differences between EDDY and CTRL (shading). Zonal wind differences that are significant at the 95% level are stippled with black dots.

can be related to the decrease in surface latent heat flux (Fig. 4c) and the decrease of specific humidity at low levels (see Fig. 6b). For $3000 < y < 5000$ km, the increase in convective precipitation can be associated with stronger convection over warm oceanic eddies and relatively weaker convection over cold eddies (not shown), as also noted by Liu et al. (2018). Since oceanic eddies are stationary in time, one may wonder if moist convection is persistent in time over warm eddies. As shown in instantaneous snapshots (Figs. 3e,f), this is obviously not the case. It is also confirmed by the fact that the frequency of rain occurrence (defined as 12-h periods with more than

1.5 mm of precipitation) remains less than 65% everywhere, including above the warmest eddies.

c. Tropospheric response

Figure 5 shows the difference in zonal-mean zonal wind (\bar{u}) between EDDY and CTRL. A clear signal is found that extends through the troposphere with its maximum near the tropopause. The order of magnitude of differences between EDDY and CTRL is 1 m s^{-1} , which may seem weak compared to the internal variability of the atmosphere, but these differences are significant at the 95% level in most regions (Fig. 5). The net effect of oceanic eddies at large scales is a poleward displacement of the jet, which affects both its barotropic and baroclinic components. Over the oceanic eddies (near $y = 4500$ km), the meridional band of easterly surface winds broadens poleward.

Figure 6a shows the EDDY – CTRL differences in zonal and time mean temperature (\bar{T}). Significant warming (between 0.2 and 0.5 K) affects the whole troposphere above a large band of latitudes between $y = 3700$ and 6000 km. This region encompasses the warm flank of the SST front where surface heat fluxes and convective precipitation are increased (Figs. 4c,d) as well as the cold flank ($y > 4500$ km), which is much less affected by this increase. The tropospheric heating is accompanied by a poleward displacement of meridional heat fluxes ($\overline{v'T'}$) (cf. Figs. 6a and 2a). This implies that the net heating of the atmosphere is not due just to upright convection over oceanic eddies but also to a large-scale modification of the circulation. Note that the response preserves at first order the thermal wind

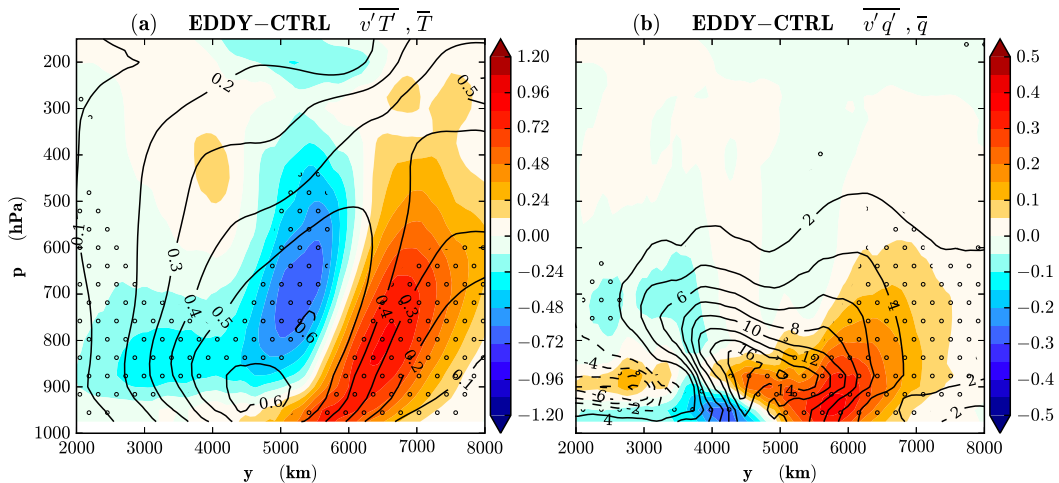


FIG. 6. Zonal and time average of EDDY – CTRL differences in (a) $\overline{v'T'}$ (shading; K m s^{-1}) and temperature (contours; K) and (b) $\overline{v'q'}$ (shading; $\text{g kg}^{-1} \text{ m s}^{-1}$) and specific humidity (contours; $10^{-2} \text{ g kg}^{-1}$). Regions with significant differences in $\overline{v'T'}$ in (a) or $\overline{v'q'}$ in (b) are stippled with black dots.

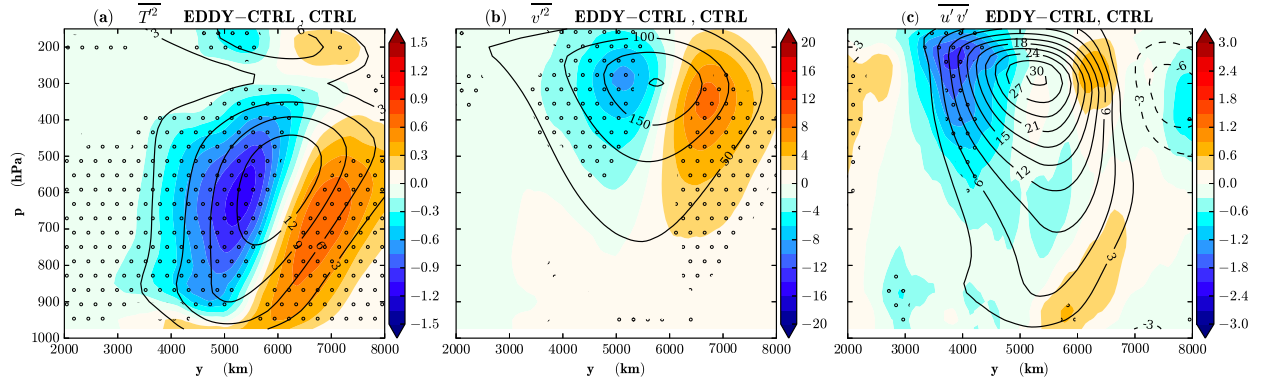


FIG. 7. As in Fig. 5, but for (a) $\langle T'T' \rangle$ (K^2), (b) $\langle v'v' \rangle$ ($\text{m}^2 \text{s}^{-2}$), and (c) $\langle u'v' \rangle$ ($\text{m}^2 \text{s}^{-2}$). Regions with significant variance differences are stippled with black dots.

balance so that the modification of the baroclinic structure of the jet is consistent with the modification of the meridional temperature gradient (not shown).

Figure 6b shows the EDDY – CTRL differences in specific humidity and meridional specific humidity flux $\langle v'q' \rangle$. A net increase in specific humidity, on the order of 0.1 g kg^{-1} , extends away from the oceanic eddying region toward the pole and above the boundary layer up to the midtroposphere. The decrease of the meridional specific humidity flux at latitudes below the SST front and its increase at higher latitudes can be interpreted as a poleward shift of the meridional flux.

Figure 7 presents the modification of the Eulerian storm track, through changes in temperature and meridional velocity variance and eddy momentum flux. Differences in temperature variance $\langle T'T' \rangle$, linked to eddy available potential energy, reach values up to 10% of the maximum magnitude of CTRL. They exhibit a typical dipolar structure, corresponding to a poleward displacement from the CTRL position (Fig. 7a). Differences in meridional velocity variance $\langle v'v' \rangle$, linked to kinetic energy, follow the same pattern of a poleward displacement at constant magnitude (Fig. 7b). The differences in eddy momentum flux $\langle u'v' \rangle$ have negative values southward of the jet around $y = 4000 \text{ km}$ and positive ones around $y = 6200 \text{ km}$ (Fig. 7c). These values are consistent with the poleward shift of the barotropic part of the zonal jet, as would be expected from an eddy feedback. However the EDDY – CTRL differences are not statistically significant, and this result should be taken with caution.

5. Mechanism of large-scale response

a. Total diabatic heating budget

Through air–sea fluxes, the direct effect of oceanic eddies is to locally warm the atmospheric boundary layer above them at latitudes between 4000 and 5000 km. An indirect effect is a net heating occurring poleward within the storm-track region, which remains to be explained. To this end, we examine the heat budget for EDDY and CTRL experiments.

The time-tendency equation for absolute temperature T in pressure coordinates is

$$\frac{\partial T}{\partial t} + \nabla \cdot (\mathbf{u}T) + \frac{\partial(\omega T)}{\partial p} - \frac{\kappa \omega T}{p} = \frac{Q_{\text{diab}}}{c_p} + \frac{R}{c_p}, \quad (1)$$

where $\mathbf{u} = (u, v)$ is horizontal velocity, and ω is vertical velocity in a pressure coordinate. Also, R is the radiative forcing, and Q_{diab} the diabatic heating resulting from latent heat release, parameterized convection, and boundary layer mixing; $c_p = 1004 \text{ J kg}^{-1} \text{ K}^{-1}$ is specific heat of dry air and $\kappa = 2/7$.

We then proceed by decomposing any variable X in a time and zonal mean $\langle \bar{X} \rangle$ (at constant pressure p), stationary spatial anomalies \bar{X}^* and the residual X^- , so that

$$X(x, y, p, t) = \langle \bar{X} \rangle(y, p) + \bar{X}^*(x, y, p) + X^-(x, y, p, t).$$

With these definitions, $\langle \bar{X}^* \rangle = \langle X^- \rangle = \bar{X}^- = 0$. Taking the zonal and time average of (1) gives

$$\begin{aligned} 0 = & \frac{\langle \bar{Q}_{\text{diab}} \rangle}{c_p} + \frac{\langle \bar{R} \rangle}{c_p} - \langle \bar{\omega} \rangle \left(\frac{\partial \langle \bar{T} \rangle}{\partial p} - \frac{\kappa \langle \bar{T} \rangle}{p} \right) - \frac{\partial \langle \bar{v}^- T^- \rangle}{\partial y} - \left(\frac{\partial \langle \bar{\omega}^- T^- \rangle}{\partial p} - \frac{\kappa \langle \bar{\omega}^- T^- \rangle}{p} \right) \\ & - \langle \bar{v} \rangle \left\langle \frac{\partial \bar{T}}{\partial y} \right\rangle - \frac{\partial \langle \bar{v}^* \bar{T}^* \rangle}{\partial y} - \left(\frac{\partial \langle \bar{\omega}^* \bar{T}^* \rangle}{\partial p} - \frac{\kappa \langle \bar{\omega}^* \bar{T}^* \rangle}{p} \right) + \text{Res.}, \end{aligned} \quad (2)$$

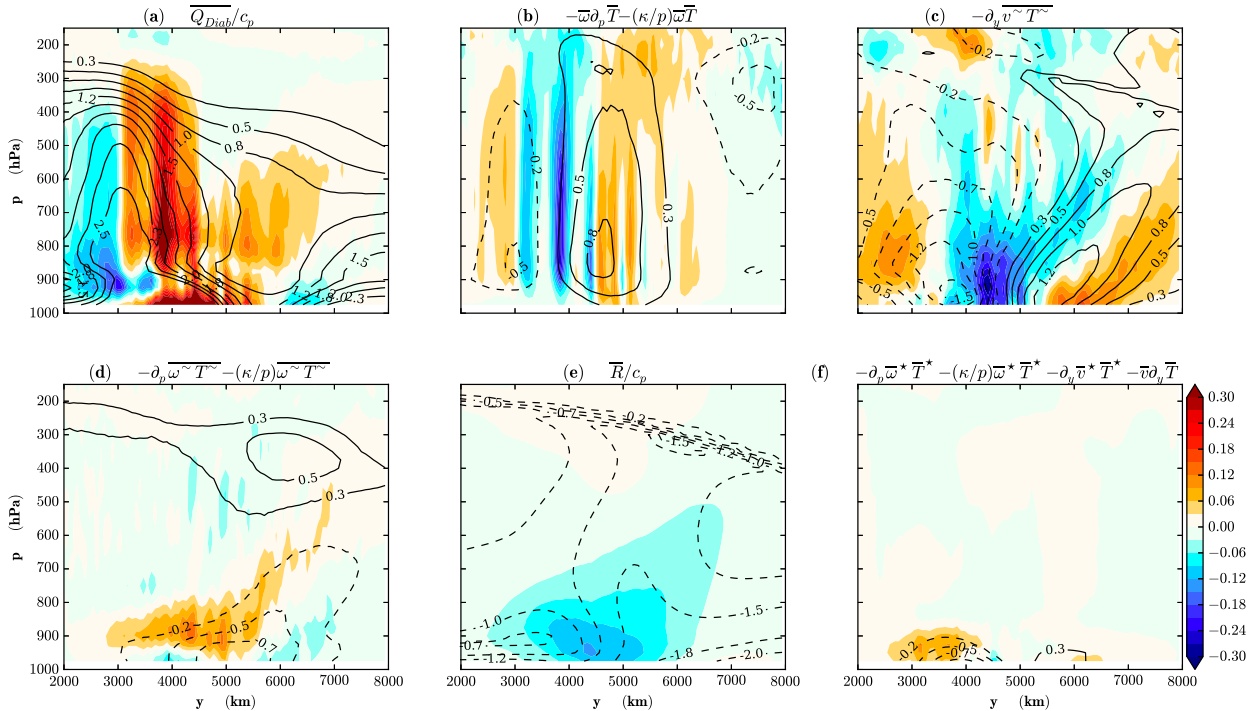


FIG. 8. (a)–(f) Zonal and time average of terms in the temperature budget [see (2); K day^{-1}] for differences between EDDY and CTRL (shading) and CTRL (contours).

where we used $\partial\langle\bar{v}\rangle/\partial y + \partial\langle\bar{w}\rangle/\partial p = 0$. The first two terms on the rhs of (2) are related to diabatic sources or sinks. The third term is related to the heat advection and adiabatic expansion by the time-mean vertical circulation. The next two terms are related to the horizontal and vertical heat fluxes due to the transients. The remaining terms correspond to the advection by the mean horizontal circulation and to temperature fluxes by stationary anomalies, as well as residual terms (due to numerics).

The different terms in (2) are shown in Fig. 8 for the CTRL experiment, as well as their EDDY – CTRL differences. First, the terms forming the second line of (2) are small (Fig. 8f), except for the EDDY – CTRL term $\partial\langle\bar{w}^*T^*\rangle/\partial p - \kappa\langle\bar{w}^*T^*\rangle/p$. This term is related to zonal asymmetries of the time-mean vertical circulation due to oceanic eddies and is confined to the boundary layer ($p < 900$ hPa).

In CTRL, diabatic heating Q_{diab} due to latent heat release as well as turbulent and convective exchanges provides a heat source near the surface and in the free troposphere on the warm side of the oceanic front (Fig. 8a). A mean vertical circulation takes place over the SST front, which warms the troposphere up to the tropopause poleward of the maximum heating (Fig. 8b). This mean circulation corresponds in part to a direct response to the large-scale SST front as explained by

Minobe et al. (2008) or Brachet et al. (2012). These terms are balanced by horizontal and vertical heat transports (Figs. 8c,d) toward high latitude and altitude, and by radiative forcing (Fig. 8e), which cools the entire troposphere.

We now consider the EDDY – CTRL differences in term of diabatic heating Q_{diab} (Fig. 8a). At latitudes lower than 3000 km, oceanic eddies are responsible for a net cooling of the troposphere. It may be associated with a reduction of water vapor at those latitudes as well as a reduction of sensible heat air–sea fluxes (Fig. 4c), which inhibit convection. On the warm side of the SST front in the region of oceanic eddies ($3000 < y < 4500$ km), a deep heating in the time mean extends up to the tropopause. At higher latitudes ($y \geq 5000$ km), the response is confined in the midtroposphere (between 850 and 500 hPa), with weaker amplitude. It is mainly due to large-scale condensation and is significant in a statistical sense up to $y \approx 8000$ km (not shown).

The modification of the mean vertical circulation by oceanic eddies induces an adiabatic cooling above the warm flank of the SST front ($y < 4500$ km) and a warming on the other side (Fig. 8b). Such a response is similar to an increase in the SST gradient that would enhance vertical motions (Minobe et al. 2008). Indeed, ascending motions above the warm flank are increased by $+0.4 \text{ mm s}^{-1}$ in the presence of eddies (not shown).

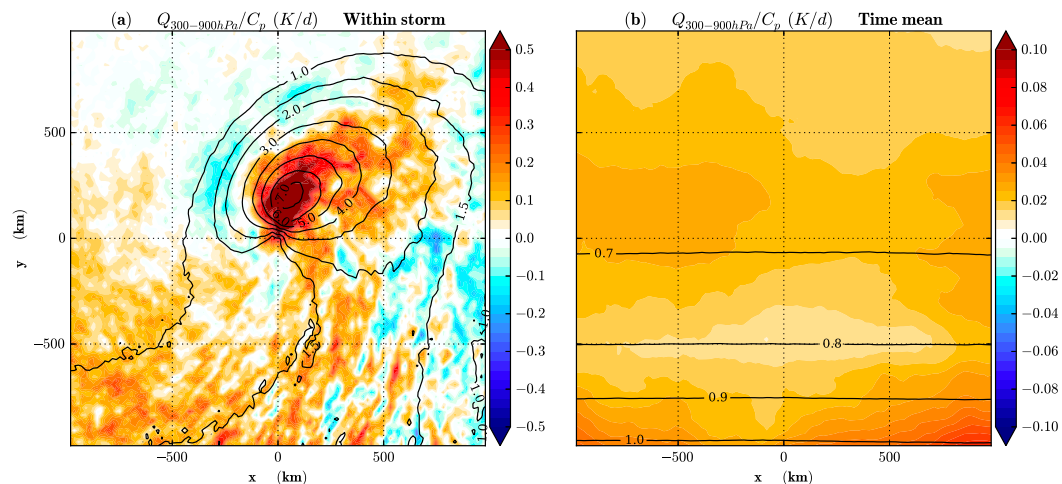


FIG. 9. (a) Composites of diabatic heating (contours; K day^{-1} ; vertically averaged between 900 and 300 hPa) for low pressure systems and the EDDY – CTRL difference (shading; K day^{-1}). (b) As in (a), but using time-mean diabatic heating instead of instantaneous values. Axes correspond to distances from the SLP minimum (km).

These two additional sources of heating are balanced by two terms: a broad radiative cooling (Fig. 8e) that is roughly opposed to the increase in mean temperature $\langle \bar{T} \rangle$ (cf. with Fig. 6a). It occurs not only in the center of the domain above the eddies but also farther poleward. Also, the divergence of meridional heat flux by the transients contributes to redistribute heat horizontally (Fig. 8c), both poleward and equatorward.

b. Diabatic heating at atmospheric synoptic scales

A possible explanation of the mean diabatic heating found in the storm-track region can be proposed following Deremble et al. (2012). Because of the presence of oceanic eddies and their net effect on surface fluxes, more water vapor is supplied to the atmosphere on the warm side of the SST front (see Fig. 4c). It is then transported poleward and upward by the synoptic atmospheric perturbations, as can be seen by an increase in meridional flux of water vapor (Fig. 6b). There, it condenses in altitude, giving rise to an increase in stratiform precipitation for $y > 5000$ km (Fig. 4d) and releasing latent heat to the atmosphere (Fig. 8a). To assess this mechanism, we compare the diabatic heating within storms for EDDY and CTRL.

Composite storms are built following general ideas of Field and Wood (2007) and Catto et al. (2010). A simple method considers local minima of sea level pressure (SLP) located within the band of latitudes between $y = 5000$ and 6000 km, with SLP values lower than 20 hPa compared to the zonal mean. A composite is created over a $2000 \text{ km} \times 2000 \text{ km}$ square box centered at the pressure minimum. No persistence in time is required, and no rotation of the fields is done to create the composite. With

these criteria, each point at these latitudes belongs to the composite domain around 15% of the time.

The composites of diabatic heating are shown in Fig. 9 for CTRL and the EDDY – CTRL difference. Here, diabatic heating is vertically averaged between 900 and 300 hPa. For the CTRL experiment, the maximum diabatic heating is located slightly northeast of the storm center and extends southward with a typical cyclonic comma shape (Fig. 9a). This is due to the warm conveyor belt (WCB) of the cyclone, which brings warm and moist air from the surface to the storm center (Carlson 1980). Because of cold temperatures at the top of the WCB, water vapor eventually condenses, releasing diabatic heating there. The diabatic heating of the EDDY – CTRL difference has a spatial structure close to CTRL, and two different regions can be distinguished (Fig. 9a). First, heating is enhanced close to the storm center, mainly due to layers between 300 and 700 hPa (not shown). We give the following interpretation for this finding. As lower atmospheric layers are moister (see Fig. 6), more water vapor is carried from the surface through the WCB. As a result, condensation occurs more often and diabatic heating increases as well in the storm center. A second region of additional diabatic heating is located in the cold sector of the storm (bottom left quadrant), which tends to reduce the strength of the cold front.

Taking the heating values of Fig. 9a and considering that it corresponds to 15% of the time, we recover typical values of the Eulerian mean (Fig. 8a). One may wonder if the additional heating within storms is in fact related to local heating above oceanic eddies in the time mean. To test this hypothesis, instead of taking instantaneous values of diabatic heating when creating the composite, we take the time-average value at the same

point in space. Figure 9b shows such a composite for CTRL and the EDDY – CTRL difference. The composite in CTRL is zonally symmetric, with typical values on the order of 1 K day^{-1} , in the range of values taken by the Eulerian time-average heating at these latitudes (Fig. 8a). The EDDY – CTRL difference is also roughly zonally symmetric with values of the order 0.1 K day^{-1} (Fig. 8a), much smaller than differences for the full diabatic heating field within the composite storm (Fig. 9a). We therefore conclude that the EDDY – CTRL difference in diabatic heating within storms is not due to permanent convection induced by oceanic eddies. This tends to validate the general picture of a large-scale transport of additional moisture by synoptic storms and diabatic heating released far away of the oceanic eddy region.

Even if a net additional heating is found in the storm centers in the EDDY experiment (Fig. 9a), we did not find significant differences in the frequency of SLP minima between EDDY and CTRL (not shown). It is consistent with the fact that the Eulerian storm track (Figs. 7a,b) is displaced poleward rather than intensified. A possible explanation can be made from the spatial organization of the additional heating (Fig. 9a). While the diabatic release of energy inside the storm increases, there is a reduction of the cold front because of a warming occurring on its cold sector. This reduction makes the frontal system less intense and may have an opposite effect, attenuating the storm.

c. Storm-track energetics

We now consider the impact of the presence of oceanic eddies on the potential energy budget, which we relate to the budget of potential temperature variance on isobaric surfaces (Lorenz 1955). Starting from (1), the tendency equation for the potential temperature variance at synoptic time scales (2–10 days) becomes, after zonal and time averaging,

$$\begin{aligned} \frac{1}{\Pi c_p} \langle \overline{Q'_{\text{diab}} \theta'} \rangle + \frac{1}{\Pi c_p} \langle \overline{R' \theta'} \rangle &= \langle \overline{v' \theta'} \rangle \frac{\partial \bar{\theta}}{\partial y} + \langle \overline{\omega' \theta'} \rangle \frac{\partial \bar{\theta}}{\partial p} \\ &+ \frac{1}{2} \frac{\partial}{\partial y} \langle \overline{v \theta'^2} \rangle + \frac{1}{2} \frac{\partial}{\partial p} \langle \overline{\omega \theta'^2} \rangle \\ &+ \frac{1}{2} \frac{\partial}{\partial y} \langle \overline{v' \theta'^2} \rangle + \frac{1}{2} \frac{\partial}{\partial p} \langle \overline{\omega' \theta'^2} \rangle + \text{Res.} \end{aligned} \quad (3)$$

Here $\Pi = (p/p_0)^\kappa$ is the Exner function. On the lhs of (3), diabatic terms correspond to sources or sinks of potential energy. On the rhs, the first term is related to the extraction of potential energy from the mean flow (also called baroclinic conversion). The second term is related to the transfer of eddy potential energy toward eddy kinetic energy (EKE), while the other terms are

associated with spatial redistribution of eddy potential energy in space. Residual terms correspond to effects due to low-frequency fluctuations (above 10 days) of the flow or to numerical dissipation.

To simplify further the budget, we use a domain-averaged reference stratification given by potential temperature Θ and Brunt–Väisälä frequency N depending only on altitude. The budget of eddy potential energy (EPE) becomes

$$\begin{aligned} 0 &= \underbrace{\frac{S}{c_p \Pi} \langle \overline{Q'_{\text{diab}} \theta'} \rangle}_{(A)} - \underbrace{S \langle \overline{\theta' v'} \rangle \frac{\partial \langle \bar{\theta} \rangle}{\partial y}}_{(B)} - \underbrace{\left\langle \overline{\omega' \frac{\partial \phi}{\partial p}} \right\rangle}_{(C)} \\ &\quad - \underbrace{\frac{\partial}{\partial y} \langle \overline{v \text{EPE}} \rangle - \frac{\partial}{\partial y} \langle \overline{v' \text{EPE}} \rangle + \frac{S}{c_p \Pi} \langle \overline{R' \theta'} \rangle + \text{Res.}}_{(D)}, \end{aligned} \quad (4)$$

using the hydrostatic approximation and with $\text{EPE} = S\theta'^2/2$, $S = g^2/(\Theta^2 N^2)$, and ϕ being the geopotential.

The different terms of the 2–10-day filtered EPE budget are summarized in Fig. 10 for CTRL (in contours). Perturbations extract energy from the zonal mean baroclinic flow through the baroclinic conversion term B, with a maximum at a latitude around $y = 6000 \text{ km}$ (Fig. 10a). A second source of eddy potential energy is due to latent heat release (term A) and is also intensified around the same latitude, at the location of the storm track (cf. Fig. 10c). Another region of EPE generation by diabatic heating is located farther equatorward, around $y = 2000 \text{ km}$, associated with deep upright convection within strong cyclonic structures (not shown). The total generation of EPE is locally balanced in large part by conversion into eddy kinetic energy [term C in (4); Fig. 10b]. The sum of the remaining terms (term D) in the EPE budget (Fig. 10d) corresponds to a sink of EPE at the core of the storm track, with similar contributions of radiative forcing and redistribution toward the polar side of the domain (not shown).

Differences between EDDY and CTRL budgets are represented by shadings in Fig. 10. Baroclinic conversion [term B in (4)] appears to be the term with the largest variation and exhibits a clear displacement toward higher latitudes (Fig. 10a). This displacement is consistent with the poleward shift of the storm track (Figs. 6 and 7). The contribution of diabatic heating to the change in the storm-track energetics (term A; cf. Fig. 10c) shows a similar poleward shift. As for the CTRL experiment, the increase in EPE generation on the poleward flank of the SST front in EDDY – CTRL is balanced in similar proportions by conversion to EKE (term C; cf. Fig. 10b), meridional transport by the perturbations and the mean flow, and radiative forcing (term D; cf. Fig. 10d).

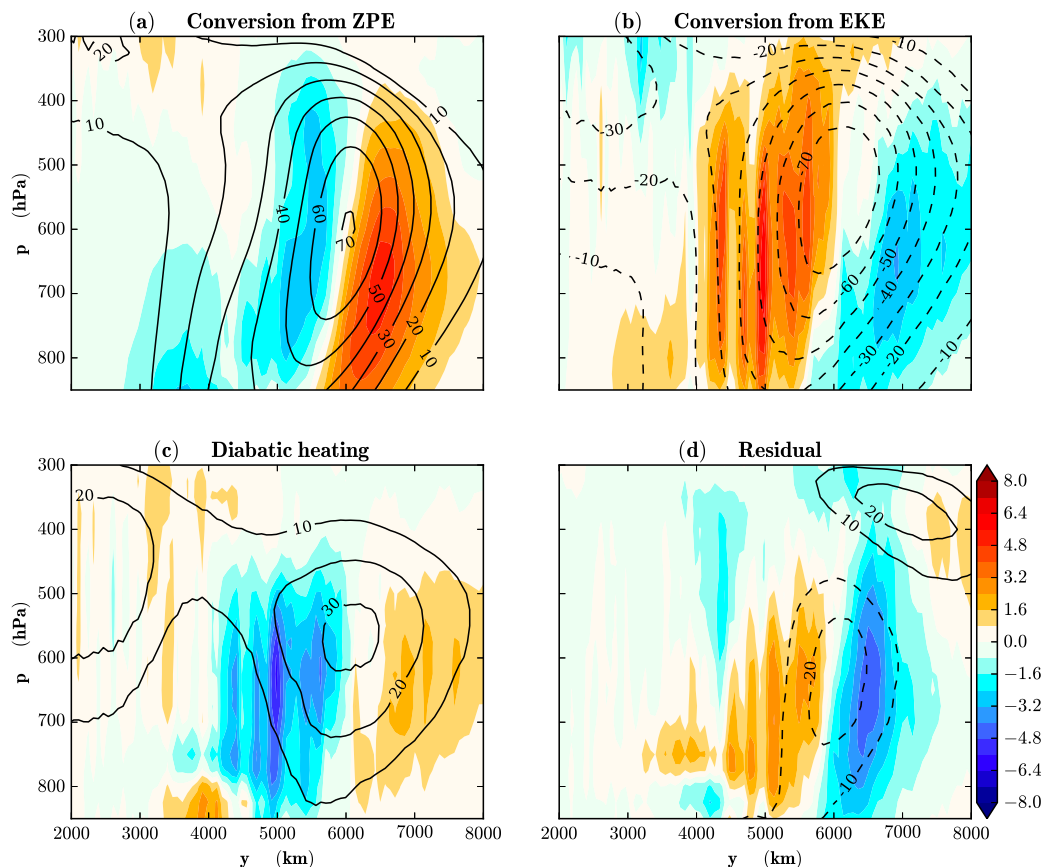


FIG. 10. (a)–(d) Zonal and time average of terms in the potential energy budget [see (4); $\text{m}^2 \text{s}^{-2} \text{day}^{-1}$] for differences between EDDY and CTRL (shading) and CTRL (contours).

Changes in baroclinic conversion are associated either with changes in mean baroclinicity (or equivalently to the Eady growth rate) or with changes in meridional heat fluxes. To separate the two effects, we decompose the variation in $S\langle v'\theta' \rangle \partial \langle \bar{\theta} \rangle / \partial y$ into

$$\begin{aligned}
 - \left[S \overline{v'\theta'} \frac{\partial \langle \bar{\theta} \rangle}{\partial y} \right]_{E-C} &= - \left[\sqrt{S} \frac{\partial \langle \bar{\theta} \rangle}{\partial y} \right]_{E-C} \left[\sqrt{S} \overline{\theta'v'} \right]_C \\
 &\quad - \left[\sqrt{S} \langle \overline{\theta'v'} \rangle \right]_{E-C} \left[\sqrt{S} \frac{\partial \langle \bar{\theta} \rangle}{\partial y} \right]_C + \text{res.},
 \end{aligned} \tag{5}$$

with $[\]_{E-C}$ being the difference between EDDY and CTRL, while $[\]_C$ corresponds to the value of the CTRL experiment and “res.” represents extra terms of smaller magnitude.

The first term on the rhs of (5) represents changes in baroclinic conversion induced by changes in mean baroclinicity at fixed meridional heat flux. It can be interpreted as the direct response of the storm track to the net tropospheric heating induced by the oceanic eddies. The second term represents changes in baroclinic

conversion induced by changes in meridional heat fluxes at fixed baroclinicity. It represents an indirect response through eddy feedbacks.

As shown by Fig. 11, the two terms on the rhs of (5) resemble the total conversion, with changes induced by a meridional heat flux of a larger amplitude than changes induced by baroclinicity. This decomposition shows that the direct response induced by the additional heating of the troposphere drives the poleward shift of the EPE generation (Fig. 11a). Then the indirect response, through positive eddy feedback, reinforces this meridional shift as shown by Fig. 11b, giving rise of the northward displacement of potential energy generation, and potential energy as well.

d. Additional experiment

Starting from the net increase in surface fluxes, previous interpretations do not invoke the spatial structure of SST anomalies. We conducted an additional experiment to determine to what extent the effect of the oceanic eddies can be interpreted as the response to a large-scale source of heat and moisture at the surface. This

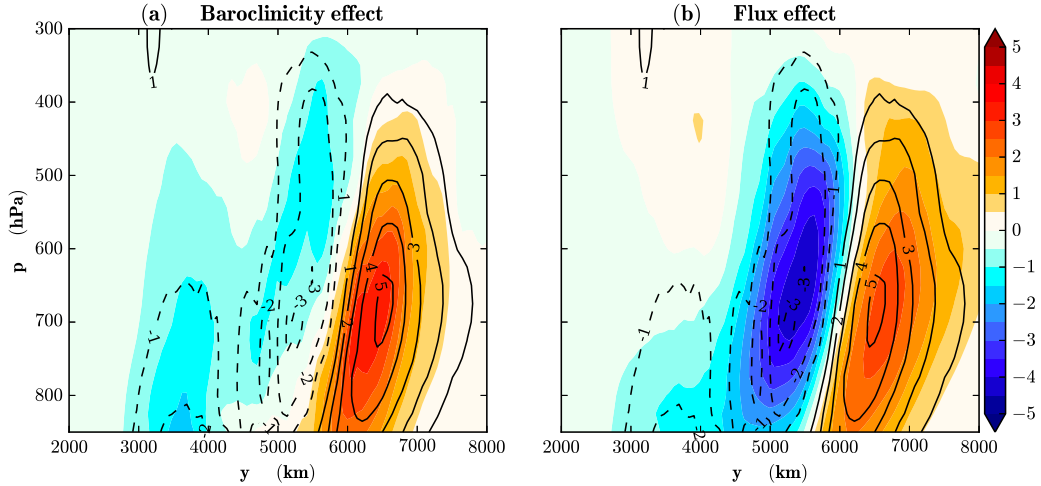


FIG. 11. EDDY-CTRL differences ($\text{m}^2 \text{s}^{-2} \text{day}^{-1}$) decomposed into (a) a change in Eady growth rate at constant heat flux and (b) a change in heat flux at constant Eady growth rate. Contours represent the total baroclinic conversion in the 2–10-day band.

experiment (FRONT) includes a modified SST profile that mimics the additional heat and moisture fed by the oceanic eddies at the core of the SST front. We keep the same shape and amplitude as the ones in CTRL, but with a northward shift by $\delta y_{\text{sst}} = 150$ km:

$$\text{SST}_{\text{FRONT}}(y) = \text{SST}_{\text{front}} - \frac{\Delta \text{SST}}{2} \tanh\left(\frac{y - y_{\text{sst}} - \delta y_{\text{sst}}}{l_{\text{sst}}}\right).$$

Given that $\delta y_{\text{sst}} \ll l_{\text{sst}}$, the SST difference between the two experiments is well approximated by

$$\begin{aligned} & \text{SST}_{\text{FRONT}} - \text{SST}_{\text{CTRL}} \\ & \approx \frac{\Delta \text{SST}}{2} \frac{\delta y_{\text{sst}}}{l_{\text{sst}}} \left\{ 1 - \left[\tanh\left(\frac{y - y_{\text{sst}}}{l_{\text{sst}}}\right) \right]^2 \right\}. \end{aligned}$$

The SST difference is thus centered on the SST front, with a maximum difference slightly below 1.5 K. The decrease away from the front resembles the envelope of the oceanic anomalies of the EDDY experiment, but exact analytical expressions differ. The value of δy_{sst} is set so that surface turbulent heat fluxes for FRONT – CTRL are comparable to the EDDY – CTRL difference. This new SST profile is used only in the surface turbulent fluxes calculation. The radiative scheme used to force the simulation remains unchanged with SST_{CTRL} as the boundary condition [see (B5)]. Four 3-yr runs are done in this configuration.

Figure 12a shows the FRONT – CTRL differences in surface fluxes, along with the modification of the SST profile. Differences in surface fluxes are of the same order of magnitude as the ones for the EDDY – CTRL

case (cf. Fig. 4). However, the atmosphere is much moister ($+0.2 \text{ g kg}^{-1}$ at 850 hPa) above the warm flank of the front (not shown). A notable decrease of the latent heat flux is found at latitude $y < 3000$ km, suggesting a large-scale change in the atmospheric circulation. As in the EDDY – CTRL case, the precipitation increase in FRONT extends farther poleward compared to increase in latent heat air–sea fluxes, mainly in the form of large-scale condensation (Fig. 12b).

Up to the tropopause, the FRONT – CTRL differences in mean temperature (Fig. 13) are similar to EDDY – CTRL, although the maximum increase is located at the surface instead of at the top of the boundary layer. Warming larger than 0.3 K extends up to the tropopause over a broad range of latitudes (3000–6000 km). The FRONT – CTRL differences in meridional eddy heat flux have more resemblance to a broadening of the region of positive values than to a poleward shift of the heat flux (cf. Figs. 13 and 2a).

Figure 14 shows FRONT – CTRL differences in perturbation kinetic and potential energies in the synoptic band. There is a high resemblance with the EDDY – CTRL differences (Figs. 7a,b), with a poleward shift of the storm track. Differences in the tendency terms in EPE budget are also roughly similar to the EDDY – CTRL case (not shown). The response of the zonal jet in the presence of a shifted SST front is shown in Fig. 15 and should be compared with Fig. 5. A comparable poleward shift of the baroclinic jet is obtained although its barotropic component seems to accelerate close to the jet core.

The response obtained for the FRONT – CTRL case is consistent with the response to heating on the

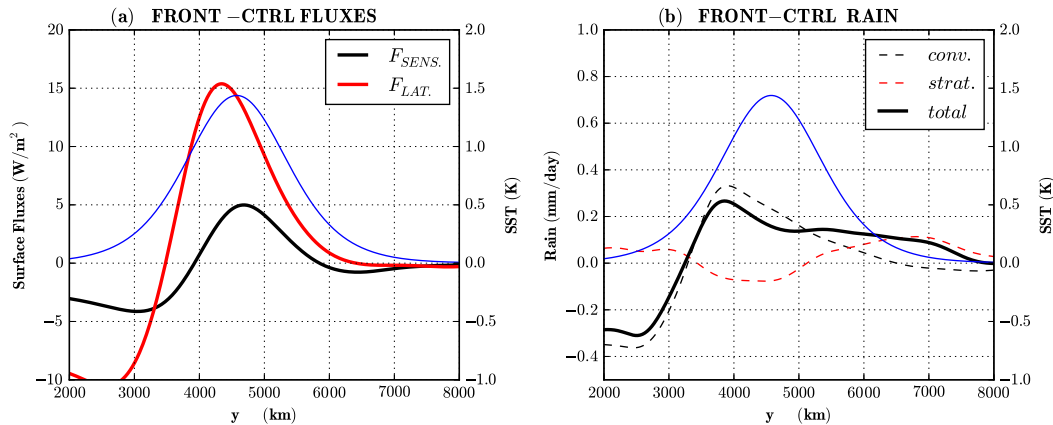


FIG. 12. As in Figs. 4c and 4d, but for FRONT – CTRL. The blue curve shows the SST difference as a function of latitude (K).

poleward side of the tropospheric jet, for both the barotropic and baroclinic components (Baker et al. 2017). In conclusion the FRONT simulation suggests that the response to the oceanic eddies can be interpreted as a response to an additional heat source at the lowest atmospheric layers.

6. Conclusions

We have examined the sensitivity of a midlatitude storm track to the presence of oceanic eddies of typical scales around 300 km. To this end, we used an idealized configuration of a zonal reentrant atmospheric channel above a SST field composed of a large-scale meridional front and of mesoscale anomalies localized over this front. Numerical simulations using the WRF model showed that the tropospheric jet shifts poleward, as well as the storm track, in the presence of oceanic eddies. This is accompanied by a net convective heating above the oceanic eddies and a poleward heating in the mid-troposphere due to diabatic heating within storms. The mechanism follows Deremble et al. (2012). Evaporation is enhanced by the presence of oceanic eddies, which moistens the boundary layer. Then atmospheric storms carry water vapor upward and poleward where latent heat is eventually released.

An additional experiment was performed to mimic the effect of the oceanic eddies by modifying the zonal mean profile of the SST field. This modification was designed to have a zonally symmetric SST field inducing surface heat fluxes with zonal mean values similar to those of the simulation with eddies. We found an atmospheric response qualitatively similar to the simulation with oceanic eddies with a meridional shift of the storm track. We conclude that the main effect of oceanic eddies can be conceived as a response to their impact in

the boundary layer, not at the scale of the eddies, but at the basin scale.

Following ideas of Peng and Robinson (2001), the atmospheric response to an extratropical SST anomaly may be decomposed into two parts: a direct linear response to the heating, mostly baroclinic, and an indirect response that would project the internal variability of the atmosphere. Actually, the change in zonal wind is in thermal wind balance with the net warming of the troposphere (not shown), which suggests the existence of a direct response. Concerning the indirect response, the eddy momentum fluxes are consistent with atmospheric perturbations tending to shift poleward the barotropic jet. However, the change in eddy momentum fluxes is relatively weak and does not pass the statistical test. This suggests that the direct response dominates in our case with a weak feedback by atmospheric eddies.

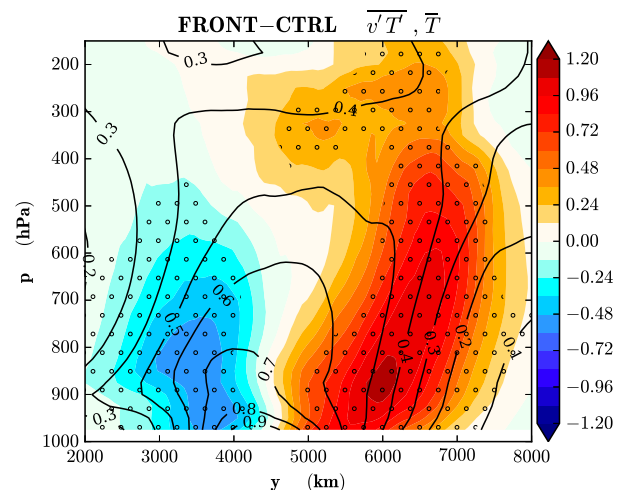


FIG. 13. As in Fig. 6a, but for FRONT – CTRL.

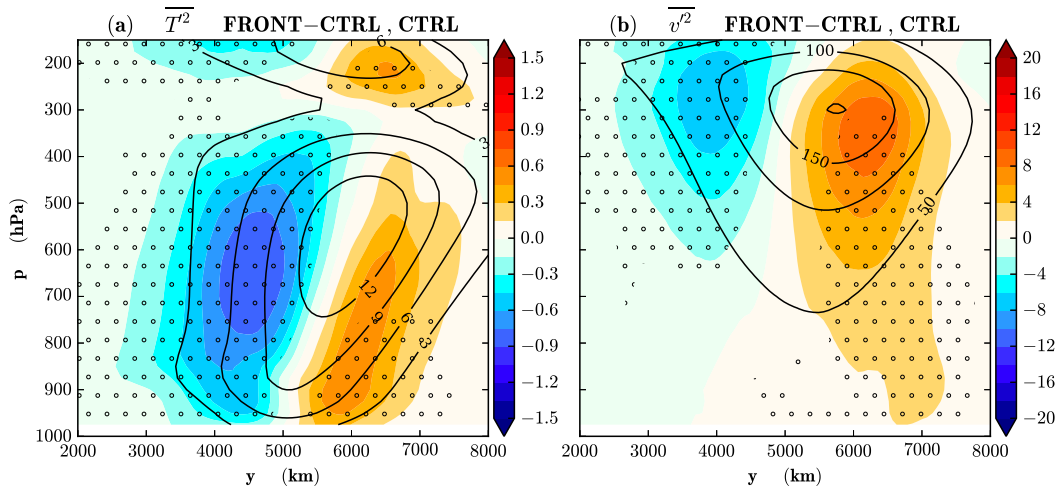


FIG. 14. As in Figs. 7a and 7b, but for FRONT – CTRL.

Our channel configuration contrasts with oceanic regions such as the Kuroshio or the Gulf Stream for which the response may be different. These oceanic fronts and the related eddies are concentrated in longitude close to the entrance regions of the Pacific or Atlantic storm tracks. As a result, oceanic eddies may enhance surface heat fluxes only at the place where synoptic storms form and not during their entire life cycle. In such situations, the indirect response due to atmospheric eddy feedback is more important downstream, as was found by Ma et al. (2017) for the Pacific storm track. In our case, single storms may have a downstream response, but, given the zonal symmetry of our configuration, there is no preferential location in longitude for these storms to develop. Hence it is plausible that the channel configuration is more relevant to regions such as above the Antarctic Circumpolar Current, although a similar shift of the storm track in the eastern North Pacific was observed by X. Ma et al. (2015) when comparing simulations with and without oceanic eddies.

One related question is the possibility to parameterize the effect of oceanic eddies through a simple meridional shift of the large-scale SST fronts. The study of Su et al. (2018) shows that the additional heating due to oceanic scales between 10 and 50 km does not only occur along such fronts but much more broadly within the ocean basins (see their Fig. 4c). It then appears difficult to relate such an additional heating to a simple shift of the large-scale fronts.

Even if our study showed a robust modification of the storm track by the oceanic eddies, its effect remains modest. To further assess the confidence on our results, sensitivity simulations to different parameters have been performed. It includes the cooling of SST by 2 K over the whole domain, or the use of SST anomalies 3 times smaller. In each case, the net effect on the

zonally averaged surface fluxes appears as robust, although its magnitude may vary by a significant ratio. The poleward shift of the storm track was also found for sufficiently high values of SST anomalies. A similar net effect was also obtained using either an increased number of vertical levels in the boundary layer, a different boundary layer parameterization [the Mellor–Yamada–Nakanishi–Niino (MYNN) scheme in WRF], or without parameterization for convection. As in our case, Ma et al. (2017) found a moderate response of the Pacific storm track to oceanic eddies in the Kuroshio Extension region. These authors highlighted the high dependence on model resolution of the amplitude of the response. The numerical resolution in their study as well as in ours resolves only partially mesoscale SST (only scales above 50 km) and the associated air–sea heat

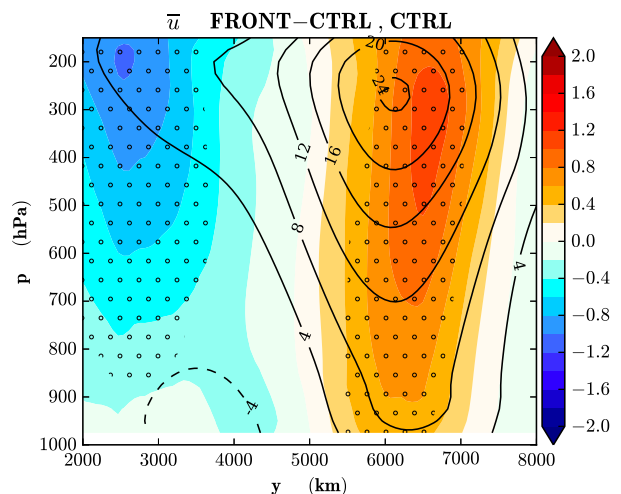


FIG. 15. As in Fig. 5, but for FRONT – CTRL.

fluxes. However, oceanic scales between 10 and 50 km give rise to a mean increase up to 4–15 W m⁻² in highly turbulent regions (Su et al. 2018). Hence, we expect much stronger surface heat fluxes in atmospheric models that will resolve such scales, with a subsequent stronger atmospheric large-scale response.

A simplification of our idealized simulations is the use of a time-independent SST, which may provide an infinite source of heat to the atmosphere. In a coupled ocean–atmosphere simulation, such an increase in surface heat fluxes should be partially reduced because of the resulting cooling of the oceanic mixed layer. An interesting follow-up to our study would be the use of coupled models to investigate how the seasonal variability of oceanic scales between 1 and 50 km (much more energetic in winter than in summer) may impact the variability of the storm track. We leave this question for future work.

Acknowledgments. This work was granted access to the HPC resources of IDRIS under the allocation A0020106852 made by GENCI (Grand Equipement National de Calcul Intensif). The authors thank Arnaud Czaja, Caroline Muller, and Gwendal Rivière for fruitful discussions about this work. We also thank Ping Chang and two anonymous reviewers who helped improve the manuscript.

APPENDIX A

Coriolis Parameter

The spatial variation of the Coriolis parameter is chosen to reproduce the Northern Hemisphere between 27° and 56°N. At the center of the domain, the Coriolis parameter equals its value at a latitude of 40°N while the β effect is at a maximum above the oceanic front, with value $\beta_{\max} = 1.75 \times 10^{-11} \text{ s}^{-1} \text{ m}^{-1}$ corresponding to its value at 40°N. The following dependence of the Coriolis parameter in y is

$$f(y) = f_0 + \beta_{\max} l_{\beta} \tanh\left(\frac{y - y_{\text{sst}}}{l_{\beta}}\right).$$

Numerical values for the above parameters (see Table 1) lead to a Coriolis parameter ranging between 0.67×10^{-4} and $1.2 \times 10^{-4} \text{ s}^{-1}$. Compared to the usual β plane, it leads to a realistic β effect in the region of interest, without extreme values of Coriolis parameter elsewhere, in particular in the equatorial side of the domain.

APPENDIX B

Radiative Model

Equations of our gray-radiation model are the same as (6)–(8) in Frierson et al. (2006). Denoting T the absolute temperature and τ the optical depth (with the convention $\tau = 0$ at the top of the atmosphere and $\tau = \tau_0$ at the surface), upward F^{\uparrow} and downward F^{\downarrow} radiative energy fluxes obey the following relations:

$$\frac{dF^{\uparrow}}{d\tau} = F^{\uparrow} - \sigma T^4, \quad (\text{B1})$$

$$\frac{dF^{\downarrow}}{d\tau} = -F^{\downarrow} + \sigma T^4, \quad (\text{B2})$$

where σ is the Stefan–Boltzmann constant. The associated diabatic term in the temperature tendency equation is

$$R = -\frac{1}{C_{\rho}\rho} \frac{\partial(F^{\uparrow} - F^{\downarrow})}{\partial z}. \quad (\text{B3})$$

We now impose the boundary conditions of the radiative fluxes such that they only depend on the SST field. We therefore impose that

$$F^{\downarrow}(\tau = 0) = 0, \quad (\text{B4})$$

$$F^{\uparrow}(\tau = \tau_0) = \sigma \text{SST}^4, \quad (\text{B5})$$

where SST is either SST_{CTRL} or SST_{EDDY} . The condition at $\tau = 0$ sets the downward radiative flux at the top of the atmosphere to zero, while the condition at $\tau = \tau_0$ corresponds to imposing a surface radiative flux that depends on SST.

Total optical depth at the surface $\tau_0(y)$ is prescribed by

$$\tau_0(y) = \tau_{\text{eq}} \cos^2\left(\frac{\pi y}{2L_y}\right) + \tau_{\text{pole}} \sin^2\left(\frac{\pi y}{2L_y}\right), \quad (\text{B6})$$

with $\tau_{\text{eq}} = 6$ and $\tau_{\text{pole}} = 1.5$. We now design the vertical dependence of optical depth $\tau(y, p)$ such that the zonal mean of temperature at radiative equilibrium (i.e., for $R = 0$) is the same for CTRL and EDDY. We also introduce two different expressions τ_S and τ_T to take into account the different behaviors in the troposphere and the stratosphere. The optical depth is then written as

$$\tau = \max(\tau_T, \tau_S), \quad (\text{B7})$$

with

$$\tau_S = \frac{1}{4} \frac{p}{p_0} \tau_0, \quad (\text{B8})$$

$$\tau_T = (1 + \tau_0) \left(\frac{p}{p_0} \right)^{4\kappa} \left[1 - \frac{\Delta\theta}{\alpha \text{SST}_{\text{CTRL}}} \log \left(\frac{p}{p_0} \right) \right]^4 - 1, \quad (\text{B9})$$

and

$$\alpha = \left[\frac{1 + \tau_0(y)}{2 + \tau_0(y)} \right]^{1/4}.$$

Note that τ_S is larger than τ_T in the highest layers, and transition from one expression to the other roughly sets the height of the tropopause in our experiments. Mean equilibrium stratification is set to $\Delta\theta = +10$ K in log pressure coordinate, stable with regard to dry convection. Table 1 summarizes the values of the various parameters used in this study.

With this choice of parameters, the potential temperature at radiative equilibrium (i.e., for $R = 0$) in the troposphere is, for the EDDY experiment

$$\theta_{\text{EDDY}}^{\text{Rad}} = \alpha \text{SST}_{\text{EDDY}} - \Delta\theta \left(1 + \frac{\text{SST}_{\text{eddies}}}{\text{SST}_{\text{front}}} \right) \log \left(\frac{p}{p_0} \right), \quad (\text{B10})$$

while in the CTRL case

$$\theta_{\text{CTRL}}^{\text{Rad}} = \alpha \text{SST}_{\text{CTRL}} - \Delta\theta \log \left(\frac{p}{p_0} \right). \quad (\text{B11})$$

It is easy to verify that $\langle \theta_{\text{EDDY}}^{\text{Rad}} \rangle = \theta_{\text{CTRL}}^{\text{Rad}}$. Also the EDDY – CTRL difference in $\langle F^1 \rangle$ at the surface in (B5) is smaller than 1 W m^{-2} , so that the change in radiative heat flux remains small at the surface.

We did sensitivity experiments by replacing the SST of the EDDY experiment by SST_{CTRL} in (B5) or replacing SST_{CTRL} by SST_{EDDY} in (B9). Even if the radiative forcing R is changed in the very first layers of the atmosphere, the change induced by oceanic eddies in the storm-track statistics was qualitatively similar in the different experiments.

REFERENCES

- Baker, H. S., T. Woollings, and C. Mbengue, 2017: Eddy-driven jet sensitivity to diabatic heating in an idealized GCM. *J. Climate*, **30**, 6413–6431, <https://doi.org/10.1175/JCLI-D-16-0864.1>.
- Bourras, D., G. Reverdin, H. Giordani, and G. Caniaux, 2004: Response of the atmospheric boundary layer to a mesoscale oceanic eddy in the northeast Atlantic. *J. Geophys. Res.*, **109**, D18114, <https://doi.org/10.1029/2004JD004799>.
- Brachet, S., F. Codron, Y. Felix, M. Ghil, H. Le Treut, and E. Simonnet, 2012: Atmospheric circulations induced by a midlatitude SST front: A GCM study. *J. Climate*, **25**, 1847–1853, <https://doi.org/10.1175/JCLI-D-11-00329.1>.
- Brayshaw, D. J., B. Hoskins, and M. Blackburn, 2008: The storm-track response to idealized SST perturbations in an aquaplanet GCM. *J. Atmos. Sci.*, **65**, 2842–2860, <https://doi.org/10.1175/2008JAS2657.1>.
- Byrne, D., L. Papritz, I. Frenger, M. Münnich, and N. Gruber, 2015: Atmospheric response to mesoscale sea surface temperature anomalies: Assessment of mechanisms and coupling strength in a high-resolution coupled model over the South Atlantic. *J. Atmos. Sci.*, **72**, 1872–1890, <https://doi.org/10.1175/JAS-D-14-0195.1>.
- Carlson, T. N., 1980: Airflow through midlatitude cyclones and the comma cloud pattern. *Mon. Wea. Rev.*, **108**, 1498–1509, [https://doi.org/10.1175/1520-0493\(1980\)108<1498:ATMCAT>2.0.CO;2](https://doi.org/10.1175/1520-0493(1980)108<1498:ATMCAT>2.0.CO;2).
- Cassou, C., and L. Terray, 2001: Dual influence of Atlantic and Pacific SST anomalies on the North Atlantic/Europe winter climate. *Geophys. Res. Lett.*, **28**, 3195–3198, <https://doi.org/10.1029/2000GL012510>.
- Catto, J. L., L. C. Shaffrey, and K. I. Hodges, 2010: Can climate models capture the structure of extratropical cyclones? *J. Climate*, **23**, 1621–1635, <https://doi.org/10.1175/2009JCLI3318.1>.
- Chang, E. K., S. Lee, and K. L. Swanson, 2002: Storm track dynamics. *J. Climate*, **15**, 2163–2183, [https://doi.org/10.1175/1520-0442\(2002\)015<0216:STD>2.0.CO;2](https://doi.org/10.1175/1520-0442(2002)015<0216:STD>2.0.CO;2).
- Chelton, D. B., M. G. Schlax, M. H. Freilich, and R. F. Milliff, 2004: Satellite measurements reveal persistent small-scale features in ocean winds. *Science*, **303**, 978–983, <https://doi.org/10.1126/science.1091901>.
- , —, and R. M. Samelson, 2011: Global observations of nonlinear mesoscale eddies. *Prog. Oceanogr.*, **91**, 167–216, <https://doi.org/10.1016/j.pocean.2011.01.002>.
- Dereemble, B., G. Lapeyre, and M. Ghil, 2012: Atmospheric dynamics triggered by an oceanic SST front in a moist quasi-geostrophic model. *J. Atmos. Sci.*, **69**, 1617–1632, <https://doi.org/10.1175/JAS-D-11-0288.1>.
- Duchon, C. E., 1979: Lanczos filtering in one and two dimensions. *J. Appl. Meteor.*, **18**, 1016–1022, [https://doi.org/10.1175/1520-0450\(1979\)018<1016:LFIOAT>2.0.CO;2](https://doi.org/10.1175/1520-0450(1979)018<1016:LFIOAT>2.0.CO;2).
- Field, P. R., and R. Wood, 2007: Precipitation and cloud structure in midlatitude cyclones. *J. Climate*, **20**, 233–254, <https://doi.org/10.1175/JCLI3998.1>.
- Frankignoul, C., N. Sennéchal, Y.-O. Kwon, and M. A. Alexander, 2011: Influence of the meridional shifts of the Kuroshio and the Oyashio Extensions on the atmospheric circulation. *J. Climate*, **24**, 762–777, <https://doi.org/10.1175/2010JCLI3731.1>.
- Frenger, I., N. Gruber, R. Knutti, and M. Münnich, 2013: Imprint of Southern Ocean eddies on winds, clouds and rainfall. *Nat. Geosci.*, **6**, 608–612, <https://doi.org/10.1038/ngeo1863>.
- Frierson, D. M., I. M. Held, and P. Zurita-Gotor, 2006: A gray-radiation aquaplanet moist GCM. Part I: Static stability and eddy scale. *J. Atmos. Sci.*, **63**, 2548–2566, <https://doi.org/10.1175/JAS3753.1>.
- Graff, L. S., and J. H. LaCasce, 2012: Changes in the extratropical storm tracks in response to changes in SST in an AGCM. *J. Climate*, **25**, 1854–1870, <https://doi.org/10.1175/JCLI-D-11-00174.1>.
- Held, I. M., S. W. Lyons, and S. Nigam, 1989: Transients and the extratropical response to El Niño. *J. Atmos. Sci.*, **46**, 163–174, [https://doi.org/10.1175/1520-0469\(1989\)046<0163:TATERT>2.0.CO;2](https://doi.org/10.1175/1520-0469(1989)046<0163:TATERT>2.0.CO;2).

- Kidston, J., A. A. Scaife, S. C. Hardiman, D. M. Mitchell, N. Butchart, M. P. Baldwin, and L. J. Gray, 2015: Stratospheric influence on tropospheric jet streams, storm tracks and surface weather. *Nat. Geosci.*, **8**, 433–440, <https://doi.org/10.1038/ngeo2424>.
- Kushnir, Y., W. Robinson, I. Bladé, N. Hall, S. Peng, and R. Sutton, 2002: Atmospheric GCM response to extratropical SST anomalies: Synthesis and evaluation. *J. Climate*, **15**, 2233–2256, [https://doi.org/10.1175/1520-0442\(2002\)015<2233:AGRTES>2.0.CO;2](https://doi.org/10.1175/1520-0442(2002)015<2233:AGRTES>2.0.CO;2).
- Kuwano-Yoshida, A., and S. Minobe, 2017: Storm-track response to SST fronts in the Northwestern Pacific region in an AGCM. *J. Climate*, **30**, 1081–1102, <https://doi.org/10.1175/JCLI-D-16-0331.1>.
- Lambaerts, J., G. Lapeyre, R. Plougonven, and P. Klein, 2013: Atmospheric response to sea surface temperature mesoscale structures. *J. Geophys. Res. Atmos.*, **118**, 9611–9621, <https://doi.org/10.1002/jgrd.50769>.
- Lapeyre, G., and P. Klein, 2006: Dynamics of the upper oceanic layers in terms of surface quasigeostrophy theory. *J. Phys. Oceanogr.*, **36**, 165–176, <https://doi.org/10.1175/JPO2840.1>.
- Lau, N.-C., 1997: Interactions between global SST anomalies and midlatitude atmospheric circulation. *Bull. Amer. Meteor. Soc.*, **78**, 21–33, [https://doi.org/10.1175/1520-0477\(1997\)078<0021:IBGSAA>2.0.CO;2](https://doi.org/10.1175/1520-0477(1997)078<0021:IBGSAA>2.0.CO;2).
- Lee, S., and H.-K. Kim, 2003: The dynamical relationship between subtropical and eddy-driven jets. *J. Atmos. Sci.*, **60**, 1490–1503, [https://doi.org/10.1175/1520-0469\(2003\)060<1490:TDRBSA>2.0.CO;2](https://doi.org/10.1175/1520-0469(2003)060<1490:TDRBSA>2.0.CO;2).
- Liu, X., P. Chang, J. Kurian, R. Saravanan, and X. Lin, 2018: Satellite-observed precipitation response to ocean mesoscale eddies. *J. Climate*, **31**, 6879–6895, <https://doi.org/10.1175/JCLI-D-17-0668.1>.
- Lorenz, E. N., 1955: Available potential energy and the maintenance of the general circulation. *Tellus*, **7**, 157–167, <https://doi.org/10.3402/tellusa.v7i2.8796>.
- Ma, J., H. Xu, C. Dong, P. Lin, and Y. Liu, 2015: Atmospheric responses to oceanic eddies in the Kuroshio Extension region. *J. Geophys. Res. Atmos.*, **120**, 6313–6330, <https://doi.org/10.1002/2014JD022930>.
- Ma, X., and Coauthors, 2015: Distant influence of Kuroshio eddies on North Pacific weather patterns? *Sci. Rep.*, **5**, 17785, <https://doi.org/10.1038/srep17785>.
- , and Coauthors, 2016: Western boundary currents regulated by interaction between ocean eddies and the atmosphere. *Nature*, **535**, 533–537, <https://doi.org/10.1038/nature18640>.
- , P. Chang, R. Saravanan, R. Montuoro, H. Nakamura, D. Wu, X. Lin, and L. Wu, 2017: Importance of resolving Kuroshio front and eddy influence in simulating the North Pacific storm track. *J. Climate*, **30**, 1861–1880, <https://doi.org/10.1175/JCLI-D-16-0154.1>.
- Michel, C., and G. Rivière, 2014: Sensitivity of the position and variability of the eddy-driven jet to different SST profiles in an aquaplanet general circulation model. *J. Atmos. Sci.*, **71**, 349–371, <https://doi.org/10.1175/JAS-D-13-074.1>.
- Minobe, S., A. Kuwano-Yoshida, N. Komori, S.-P. Xie, and R. J. Small, 2008: Influence of the Gulf Stream on the troposphere. *Nature*, **452**, 206–209, <https://doi.org/10.1038/nature06690>.
- Nakamura, H., T. Sampe, Y. Tanimoto, and A. Shimpo, 2004: Observed associations among storm tracks, jet streams, and midlatitude oceanic fronts. *Earth's Climate: The Ocean–Atmosphere Interaction*, *Geophys. Monogr.*, Vol. 147, Amer. Geophys. Union, 329–345.
- , —, A. Goto, W. Ohfuchi, and S.-P. Xie, 2008: On the importance of midlatitude oceanic frontal zones for the mean state and dominant variability in the tropospheric circulation. *Geophys. Res. Lett.*, **35**, L15709, <https://doi.org/10.1029/2008GL034010>.
- O'Neill, L. W., 2012: Wind speed and stability effects on coupling between surface wind stress and SST observed from buoys and satellite. *J. Climate*, **25**, 1544–1569, <https://doi.org/10.1175/JCLI-D-11-00121.1>.
- O'Reilly, C. H., and A. Czaja, 2015: The response of the Pacific storm track and atmospheric circulation to Kuroshio Extension variability. *Quart. J. Roy. Meteor. Soc.*, **141**, 52–66, <https://doi.org/10.1002/qj.2334>.
- , S. Minobe, A. Kuwano-Yoshida, and T. Woollings, 2017: The Gulf Stream influence on wintertime North Atlantic jet variability. *Quart. J. Roy. Meteor. Soc.*, **143**, 173–183, <https://doi.org/10.1002/qj.2907>.
- Peng, S., and W. A. Robinson, 2001: Relationships between atmospheric internal variability and the responses to an extratropical SST anomaly. *J. Climate*, **14**, 2943–2959, [https://doi.org/10.1175/1520-0442\(2001\)014<2943:RBAIVA>2.0.CO;2](https://doi.org/10.1175/1520-0442(2001)014<2943:RBAIVA>2.0.CO;2).
- Piazza, M., L. Terray, J. Boé, E. Maisonnave, and E. Sanchez-Gomez, 2016: Influence of small-scale North Atlantic sea surface temperature patterns on the marine boundary layer and free troposphere: A study using the atmospheric ARPEGE model. *Climate Dyn.*, **46**, 1699–1717, <https://doi.org/10.1007/s00382-015-2669-z>.
- Plougonven, R., A. Foussard, and G. Lapeyre, 2018: Comments on “The Gulf Stream convergence zone in the time-mean winds.” *J. Atmos. Sci.*, **75**, 2139–2149, <https://doi.org/10.1175/JAS-D-17-0369.1>.
- Renault, L., M. J. Molemaker, J. C. McWilliams, A. F. Shchepetkin, F. Lemarié, D. Chelton, S. Illig, and A. Hall, 2016: Modulation of wind work by oceanic current interaction with the atmosphere. *J. Phys. Oceanogr.*, **46**, 1685–1704, <https://doi.org/10.1175/JPO-D-15-0232.1>.
- Révelard, A., C. Frankignoul, N. Sennéchaël, Y.-O. Kwon, and B. Qiu, 2016: Influence of the decadal variability of the Kuroshio Extension on the atmospheric circulation in the cold season. *J. Climate*, **29**, 2123–2144, <https://doi.org/10.1175/JCLI-D-15-0511.1>.
- Robinson, W. A., 2000: Review of WETS—The Workshop on Extra-Tropical SST Anomalies. *Bull. Amer. Meteor. Soc.*, **81**, 567–577, [https://doi.org/10.1175/1520-0477\(2000\)081<0567:ROWTWO>2.3.CO;2](https://doi.org/10.1175/1520-0477(2000)081<0567:ROWTWO>2.3.CO;2).
- Sampe, T., H. Nakamura, A. Goto, and W. Ohfuchi, 2010: Significance of a midlatitude SST frontal zone in the formation of a storm track and an eddy-driven westerly jet. *J. Climate*, **23**, 1793–1814, <https://doi.org/10.1175/2009JCLI3163.1>.
- Shapiro, M. A., H. Wernli, N. A. Bond, and R. Langland, 2001: The influence of the 1997–1999 ENSO on extratropical baroclinic life cycles over the eastern North Pacific. *Quart. J. Roy. Meteor. Soc.*, **127**, 331–342, <https://doi.org/10.1002/qj.49712757205>.
- Shaw, T., and Coauthors, 2016: Storm track processes and the opposing influences of climate change. *Nat. Geosci.*, **9**, 656–664, <https://doi.org/10.1038/ngeo2783>.
- Skamarock, W., and Coauthors, 2008: A description of the Advanced Research WRF version 3. NCAR Tech. Note NCAR/TN-475+STR, 113 pp.
- Small, R. J., R. A. Tomas, and F. O. Bryan, 2014: Storm track response to ocean fronts in a global high-resolution climate model. *Climate Dyn.*, **43**, 805–828, <https://doi.org/10.1007/s00382-013-1980-9>.

- Smirnov, D., M. Newman, M. A. Alexander, Y.-O. Kwon, and C. Frankignoul, 2015: Investigating the local atmospheric response to a realistic shift in the Oyashio sea surface temperature front. *J. Climate*, **28**, 1126–1147, <https://doi.org/10.1175/JCLI-D-14-00285.1>.
- Su, Z., J. Wang, P. Klein, A. F. Thompson, and D. Menemenlis, 2018: Ocean submesoscales as a key component of the global heat budget. *Nat. Commun.*, **9**, 775, <https://doi.org/10.1038/s41467-018-02983-w>.
- Tokinaga, H., Y. Tanimoto, S.-P. Xie, T. Sampe, H. Tomita, and H. Ichikawa, 2009: Ocean frontal effects on the vertical development of clouds over the western North Pacific: In situ and satellite observations. *J. Climate*, **22**, 4241–4260, <https://doi.org/10.1175/2009JCLI2763.1>.
- Vannière, B., A. Czaja, H. Dacre, and T. Woollings, 2017: A “cold path” for the Gulf Stream–troposphere connection. *J. Climate*, **30**, 1363–1379, <https://doi.org/10.1175/JCLI-D-15-0749.1>.
- Villas Bôas, A. B., O. T. Sato, A. Chaigneau, and G. P. Castelão, 2015: The signature of mesoscale eddies on the air–sea turbulent heat fluxes in the South Atlantic Ocean. *Geophys. Res. Lett.*, **42**, 1856–1862, <https://doi.org/10.1002/2015GL063105>.
- Woollings, T., B. Hoskins, M. Blackburn, D. Hassell, and K. Hodges, 2010: Storm track sensitivity to sea surface temperature resolution in a regional atmosphere model. *Climate Dyn.*, **35**, 341–353, <https://doi.org/10.1007/s00382-009-0554-3>.